

Fault Rheology Control on Rupture Propagation and Aftershocks Distribution during the 2016–2017 Central Italy Earthquakes

Pasquale De Gori^{*1}, Maddalena Michele¹, Lauro Chiaraluce¹, and Claudio Chiarabba¹

Abstract

The stress released by the large coseismic ruptures and related aftershock sequences is strongly a heterogeneous process. We show highly resolved images of the normal fault system ruptured during the 2016–2017 central Italy earthquake sequence, as obtained by the high-resolution local earthquake tomography allowing relocation of a massive set of aftershocks. We get evidence that lateral changes of elastic properties on the fault planes account for the complexity in the rupture processes during the two $M_w > 6$ earthquakes. We observe an emergent phase in the first part of the M_w 6.5 rupture, and the coseismic slip becomes large when the rupture breaks through high Poisson ratio portions of the fault. Mainshocks break the fault portions that, although limited and segmented by inherited structural complexity, were dynamically interfering during the faulting episodes. The close repetition of slip on the same relatively high Poisson ratio patch suggests a dynamic weakening of the fault and/or an incomplete stress release during the first mainshock.

Cite this article as De Gori, P., M. Michele, L. Chiaraluce, and C. Chiarabba (2023). Fault Rheology Control on Rupture Propagation and Aftershocks Distribution during the 2016–2017 Central Italy Earthquakes, *Seismol. Res. Lett.* **94**, 2642–2654, doi: [10.1785/0220220284](https://doi.org/10.1785/0220220284).

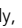



[Supplemental Material](#)

Introduction

The release of stress during large earthquakes and aftershocks is largely heterogeneous (Mai and Beroza, 2002; Ben-Zion and Sammis, 2003). Aftershocks tend to equilibrate the stress perturbation generated by large ruptures. Many observations defined the tendency of aftershocks to cluster around coseismic slip patches, for the heterogeneity of stress and elastic properties (Reasenber and Ellsworth, 1982; Mendoza and Hartzell, 1988). Stress heterogeneity can arise from the inhomogeneity in the elastic structure and the propagation of fault slip through geometric complexities. Lithological (e.g., rheological) and geometrical heterogeneities interfere with rupture propagation (Fang and Dunham, 2013) and local stresses are perturbed during the rupture evolution, producing variable fault slip, accelerations, and decelerations of the rupture front (Heaton, 1982; Beroza and Spudich, 1988; Dieterich and Smith, 2009; Shi and Day, 2013; Bruhat *et al.*, 2016; Albertini and Kammer, 2017; Cirella *et al.*, 2018). Correlation between slip behavior and change in material properties along the faults has been reported for different case studies (Michael and Eberhart-Phillips, 1991; Zhao and Negishi, 1998; Piana Agostinetti *et al.*, 2020). At a plate boundary scale, the structural heterogeneities controlled the nucleation of mega-earthquake and the rupture evolution complexity, localizing the slip, and the high-frequency radiation (Liu and Zhao, 2018). Although at crustal scale, we have the example of the 2009 M_w 6.1 L'Aquila normal-faulting

earthquake, in which the onset of the seismic rupture consisted of an emergent phase with a small moment release that has been related to heterogeneity of lithology and material properties inferred by seismic tomography (Di Stefano *et al.*, 2011).

During the 2016–2017 Amatrice-Norcia sequence, three mainshocks (the 24 August M_w 6.1, the 26 October M_w 5.9, and the 30 October M_w 6.5), and several $M_w > 5$ mainshocks spread on an 80 km north-northwest-elongated section of the normal-faulting system (Fig. 1; Chiaraluce *et al.*, 2017; Tan *et al.*, 2021). The detailed source models of the two $M_w > 6$ mainshocks have been obtained with different methods grounding on a large suite of high-resolution data and observations (Cheloni *et al.*, 2017; Huang *et al.*, 2017; Tinti *et al.*, 2016; Cirella *et al.*, 2018; Scognamiglio *et al.*, 2018). Although all the models agree with a high degree of complexity of fault geometry and slip distribution, an acceleration of the rupture front and impulsive split of rupture pulses were observed and associated with the presence of structural and stress barriers along the fault system (Chiaraluce *et al.*, 2017; Cirella *et al.*, 2018). For the two mainshocks, surface evidence indicates that the same fault

1. Istituto Nazionale di Geofisica e Vulcanologia, Rome, Italy,  <https://orcid.org/0000-0001-8160-0849> (PDG);  <https://orcid.org/0000-0001-9039-3503> (MM);  <https://orcid.org/0000-0002-9697-6504> (LC);  <https://orcid.org/0000-0002-8111-3466> (CC)

*Corresponding author: pasquale.degori@ingv.it

© Seismological Society of America

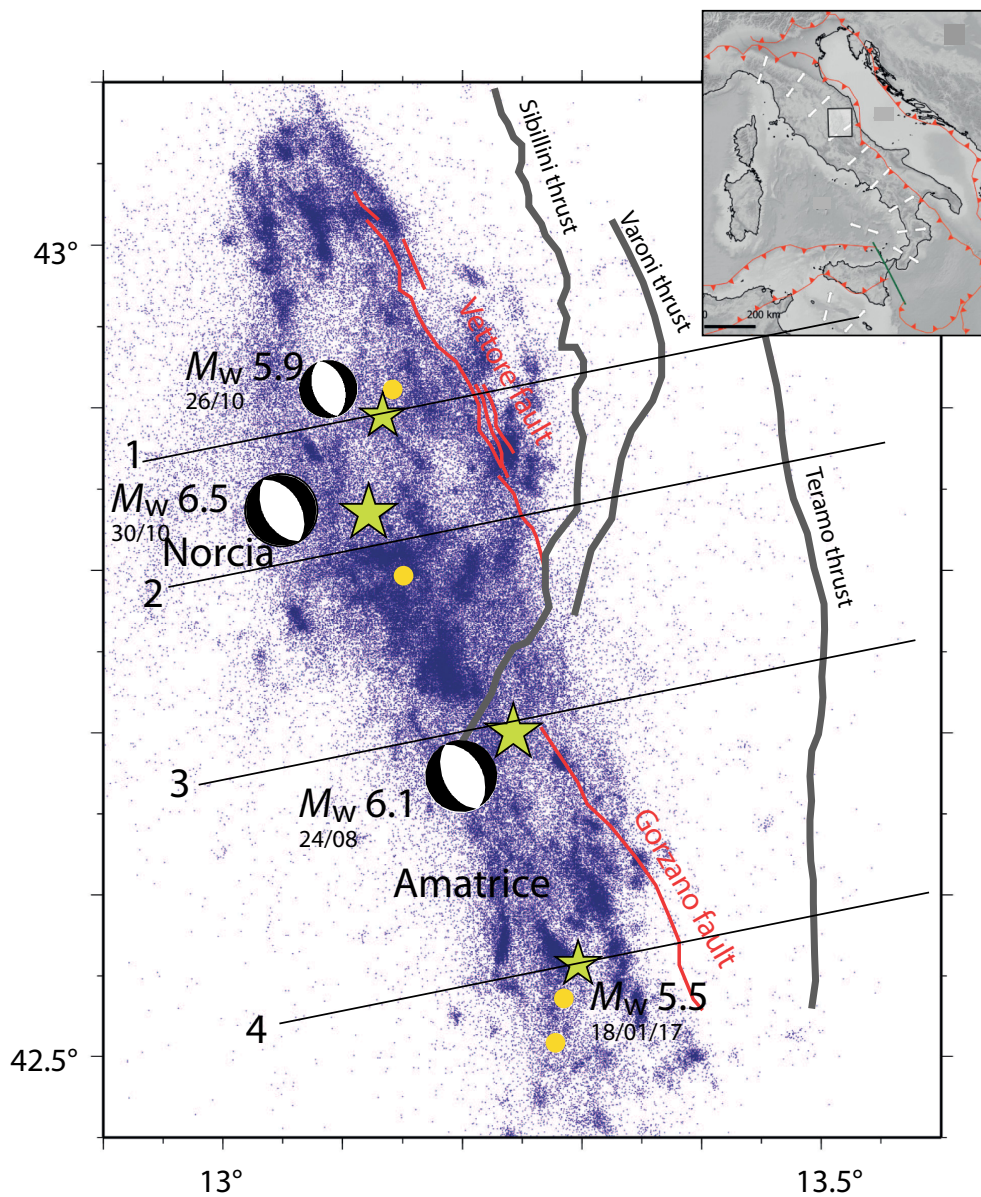


Figure 1. Map of 3D relocated seismicity: mainshocks (green stars indicate 24 August M_w 6.1, 30 October M_w 6.5, and 26 October M_w 5.9), large aftershocks (yellow circles), and aftershocks of the 2016 sequence. Centroid Moment Tensor (CMT) focal mechanisms, surface traces of normal faults (in red the Mt. Vettore fault and the Gorzano fault), main compressional thrusts (gray lines), and traces of sections in Figure 9 are shown. The upper right inset shows the geographical location of the study area (small square) with the main structural elements. The color version of this figure is available only in the electronic edition.

portion of the Vettore fault slipped during both the events (Villani *et al.*, 2018; Brozzetti *et al.*, 2019).

The complete set of aftershocks recorded during the seismic sequence is an unprecedented harvest for understanding how material properties influence the fault behavior (Improta *et al.*, 2019; Tan *et al.*, 2021; Chiaraluce *et al.*, 2022). In this study, we have computed V_p and V_p/V_s models using similar techniques and approaches as in Chiarabba *et al.* (2018), grounded on a more complete set of data including arrivals from 20

additional seismic stations located within 30 km of distance from the epicentral area (Fig. 2). Then, we have used the new 3D model to both generate novel Poisson ratio images of the faults and to relocate Spallarossa *et al.* (2021) earthquakes catalog to present a synoptic view of the fault system.

Tomographic Imaging and Aftershock Relocation

Our analysis moved from the aftershocks catalog by Spallarossa *et al.* (2021) that is among the largest ever produced for a normal-faulting earthquake sequence: it includes 440,697 automatically detected events and phase data. We compute V_p and V_p/V_s models with the SimulPS14 technique (Thurber, 1983; Eberhart-Phillips, 1990; Eberhart-Phillips and Reyners, 1997) using a subset of the well-located events, which have at least 7 P and 3 S observations, closest station within 10 km from hypocenter, location errors less than 1 km, and azimuthal gap less than 180°. This first selection gives a total of 232,856 events that are randomly reduced to 25,876 (about 10% of the overall data set) to speed up the tomographic inversion without decreasing the quality of the ray coverage within the target volume. The

method uses P and $S-P$ arrival times to solve for hypocentral and velocity (V_p and V_p/V_s) parameters with a damped least-squares inversion after solving the location-velocity coupling (Haslinger, 1998). Seismic rays of P waves are traced with a pseudobending technique and velocities are assigned and perturbed at a 3D grid of nodes with spacing of $5 \times 5 \times 3$ km (in x , y , and z). The initial velocity model is taken from Chiarabba *et al.* (2018). The inversion is done using 799,588 P -wave and 620,352 S -wave arrival times, doubling the observations for single-event

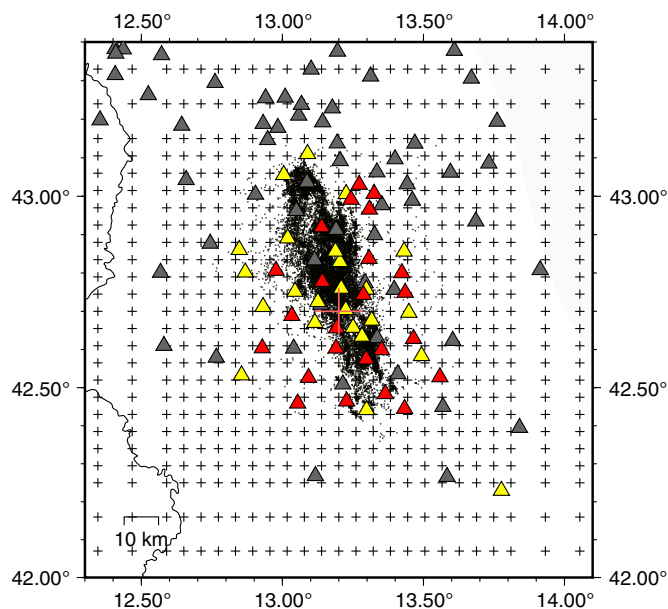


Figure 2. Earthquakes (dots) and seismic stations (gray indicates permanent INGV; yellow indicates temporary INGV; red indicates temporary British Geological Survey [BGS]) used for the inversion. Crosses are grid points of the model. The color version of this figure is available only in the electronic edition.

with respect to the model computed by Chiarabba *et al.* (2018). These new models incorporate data from additional temporary stations (red triangles in Fig. 2) previously not used, which are better covering the northern and southern terminations of the fault system. The model parameterization and damping parameters were chosen to get the highest resolved model fidelity balanced with model complexity. We get a higher improvement of data variance (44% instead of 32%) and a final root mean square (rms) of 0.2 s after five iterations. The denser covering permits the improvement of the model resolution and fidelity and extends the modeled volume.

With the new 3D models, we have relocated, using SIMULPS14, the pool of 232,856 events previously described, and compared the 3D locations with those refined with the double-difference approach (Waldhauser *et al.*, 2021). The 3D-located catalog has location errors in the range of 0.02–0.3 km for x , y , and 0.05–0.6 km for z coordinates (see Fig. 3). A comparison with precise relative locations refined with the double-difference method indicates that the overall geometry of the system is similarly revealed, whereas the relative locations collapse more strongly, improving the seismicity alignments (Fig. 4). Anyway, a first-order similarity in geometry of the main clusters in terms of trends, fault dip, and vertical extent is evident.

Velocity Model Results

The resolution of the velocity model has been assessed with a full investigation of the matrix resolution and the computation

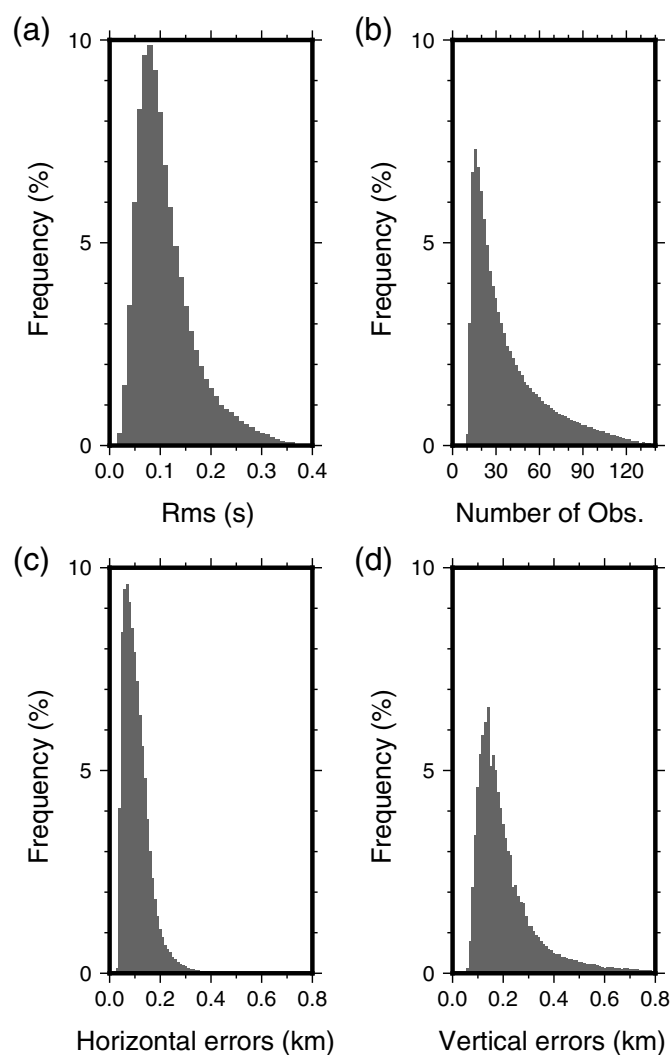
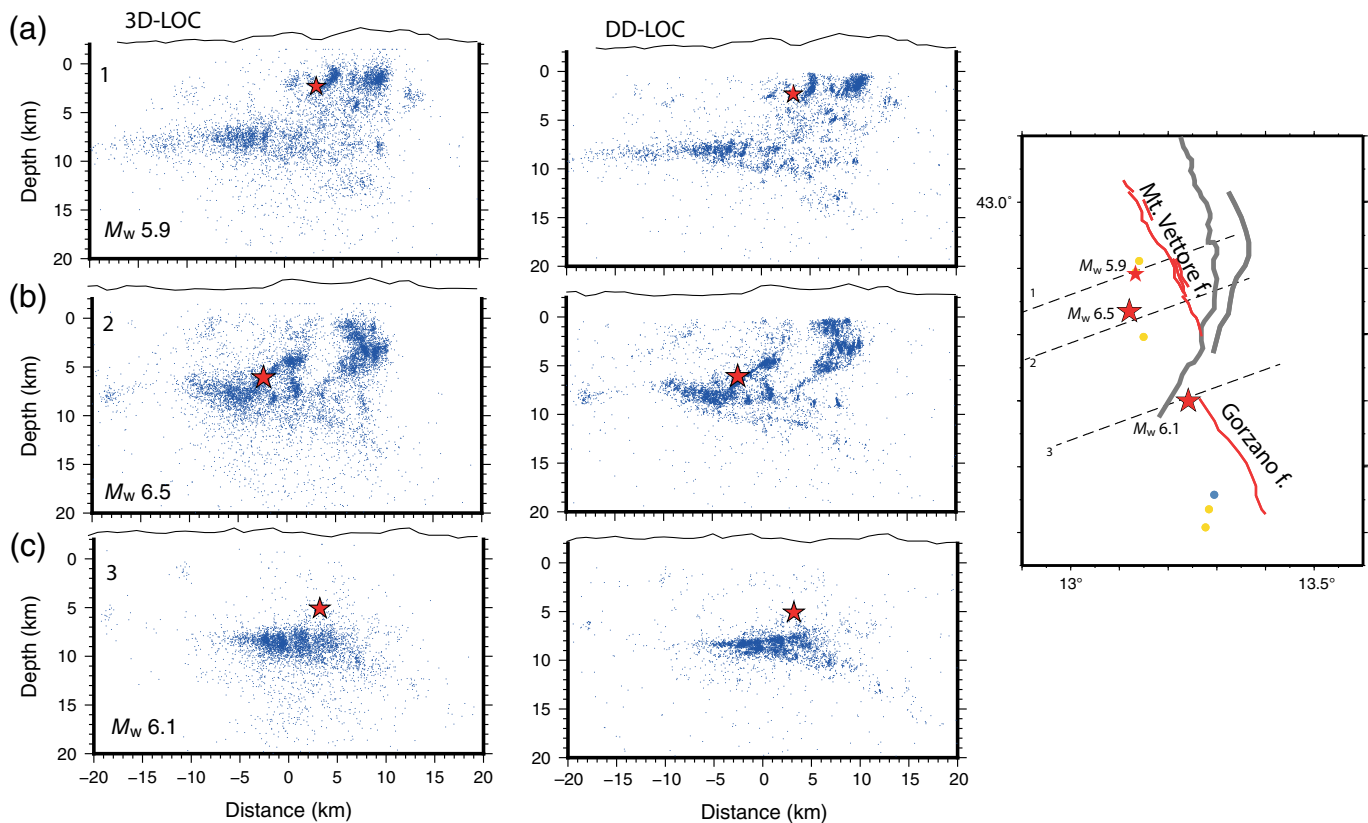


Figure 3. (a) Location root mean square (rms), (b) number of observations, and (c,d) hypocentral errors for the relocated seismicity.

of the spread function (SF, see Toomey and Foulger, 1989; Michelini and McEvelly, 1991) and with a classical checkerboard test (see the supplemental material). The optimal reproduction of synthetic features indicates the very high resolution of the model, coherently with the SF (Fig. 5).

The upper crust structure has significant V_p changes between the northern and southern sectors that probably represent major lithological variations (Fig. 6). The north-northwest trending of the high-velocity bodies at depth >3 km suggests a decoupling between shallow (i.e., the Sibillini thrust) and deep compressional structures. Apart from this broad feature, a high- V_p/V_s body persists at 3 and 6 km depth in the area, confined by the Sibillini thrust, where the two ruptures propagated and interacted.

The vertical sections are drawn across the fault system at the intersection with the two mainshocks hypocenter and at the



northern and southern terminations of the fault system at the nucleation sites of $M_w > 5$ earthquakes.

The comparison with the Chiarabba *et al.* (2018) model (Fig. 7) shows anomalies similarly distributed, but the resolution of the new model results in a more defined and resolved picture of the 3D system. In the central part, the V_p pattern is more marked with clearer features both at the northern and southern portion of the system, whereas the V_p/V_s positive anomalies are more continuously elongated along the compressional Sibillini system. The V_p values and the relatively high V_p/V_s of the upper crust is consistent with the carbonate nature of the rocks, as also evidenced in other local earthquake tomography studies of the Apennines (Improta *et al.*, 2014; Chiarabba *et al.*, 2020).

Implications for the Fault System Geometry and Mainshocks

The skeleton of the main-fault system and the geometry at depth of the major Vettore fault are well revealed by relocated seismicity (DD locations in Fig. 8 and 3D locations in Fig. 9), together with many small (tens of kilometers long) secondary segments and fault strands. The lateral continuity of the pre-existing extensional faults is limited by the stack of continental margin of Adria during the Apennines compression, in which the main feature here is the Sibillini thrust. Therefore, the reactivation of the pre-existing faults interferes with this lack of lateral continuity and the propagation of seismic ruptures is conditioned. Part

Figure 4. Comparison between the (a) 3D and (b) DD locations (Waldhauser *et al.*, 2021) for the same pool of events displayed on three vertical sections across the mainshocks: (a) M_w 5.9, (b) M_w 6.5, and (c) M_w 6.1. Earthquakes within 1 km distance from the vertical planes are projected. The number of each section is reported in the upper left corner (1, 2, and 3) of panels (a,b,c). Traces (1, 2, and 3) are shown in the map in panel (c). The color version of this figure is available only in the electronic edition.

of the seismicity aligns on the pre-existing segments in the foot-wall of the Vettore fault (Fig. 8), and reasonably part of the overall compressional edifice (Fig. 8). Seismicity is capped on a low-angle, east-dipping, basal plane located within a relatively high- V_p and low- V_p/V_s volume (Fig. 9).

The first M_w 6.1 event (section 3 in Fig. 9) consists of two main patches (slip > 50 cm; see Fig. 10) with a maximum slip of 0.8–1.0 m, located north and south of the hypocenter (Tinti *et al.*, 2016; Cirella *et al.*, 2018). No aftershocks aligned on the fault at the hypocenter location, although the fault could be evinced by a marked V_p contrast with high V_p/V_s in the hanging wall. The northern patch ruptured a steep southwest-dipping segment (section 6 in Fig. 8). Aftershocks align not only on the fault plane, but also spread on a volume around the plane, more sensibly after the second mainshock.

On 26 October, an M_w 5.9 event struck the northern portion of the fault system (section 1 in Fig. 9), five days before the

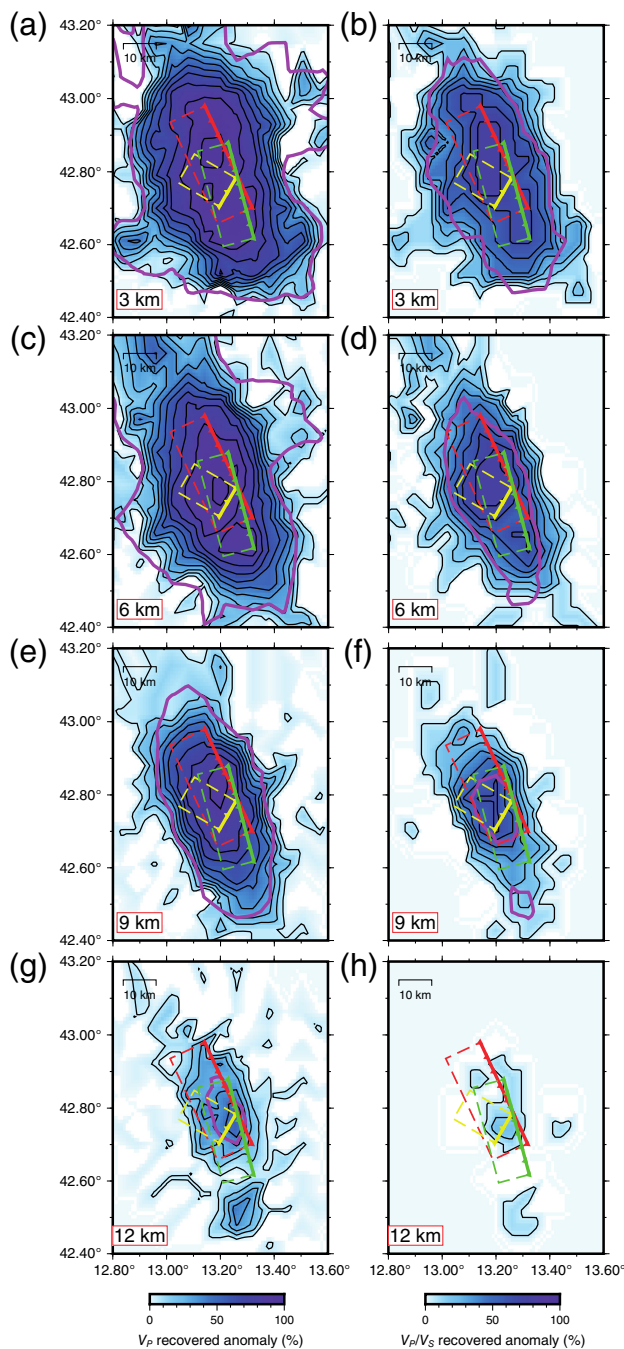


Figure 5. Results of the checkerboard recovery tests in layers 3, 6, 9, and 12 km depth for V_p (panels a, c, e, g) and V_p/V_s model (panels b, d, f, h). For each layer we show the percentage of recovered anomalies starting from synthetic anomalies of $\pm 5\%$ with respect to the 1D V_p and V_p/V_s models (standard representation in Figure SOM1). The anomalies are well recovered within most of the model and optimally ($>80\%$) around the faults (indicated by boxes). We also plot the spread function (SF) computed from the full resolution matrix. According to [Toomey and Foulger \(1989\)](#), the best way to establish the threshold of SF that provides negligible smearing effects and satisfactory node ray sampling (DWS) is to individuate the kink of the L-shaped plot defined by reporting SF versus DWS for the V_p and V_p/V_s nodes (Figure SOM2). In our case the selected values are $SF = 1.8$ and $SF = 3.0$ for V_p and V_p/V_s models, respectively. The color version of this figure is available only in the electronic edition.

second large mainshock. The event is relatively shallow and has a well-defined aftershock alignment, describing the southwest-dipping plane at the border of a high- V_p fold unit and within a high- V_p/V_s anomaly.

The M_w 6.5 event is rather complex with the activation of a main $N155^\circ$ -trending plane with a maximum slip of 2.5 m, and some secondary fault planes ([Cheloni et al., 2017](#); [Huang et al., 2017](#); [Scognamiglio et al., 2018](#)). The earthquake originated within a high- V_p and low- V_p/V_s volume at the contact with the basal east-dipping plane. Aftershocks align on the deeper part of the plane between 8 and 3 km depth, along a steep segment in the hanging wall of the thrust system splay (Fig. 8). Aftershocks align on the fault plane in the central portion (sections 1 and 2 in Fig. 8), whereas off-fault seismicity increases at the rotation of the thrust system (i.e., see the dispersion of seismicity from the fault plane in sections 3 and 4 of Fig. 8), suggesting a complexity of the rupture that we hypothesize is due to the pre-existing structural heterogeneities. The amount of seismicity occurring in the volume around the fault is high, with a deep alignment east of the fault, representing the activation of inherited structures of the compressional edifice. We observe a very emergent onset of the rupture followed a few seconds later by the large slip on the main asperity (Figure SOM3, available in the supplemental material to this article). Such rupture onset is similar to that observed for the 2009 L'Aquila mainshock ([Di Stefano et al., 2011](#)).

The southern termination of the fault system has been ruptured by several $M_w > 5$ events, the largest being an M_w 5.5 mainshock, on 18 January 2017. Aftershocks align here on a southwest-dipping plane from 5 to 10 km depth, at the border of a high- V_p body, resembling a long-lived normal fault (section 4 in Fig. 9). Earthquakes mostly clustered within high- V_p/V_s volumes, suggesting that fluid overpressure has been a process that favored the fault segments activation at the fault system termination.

Discussion

The rupture history of the two M_w 6.1 and 6.5 mainshocks is described by several articles as a heterogeneous process, with an activation of different patches on the adjoining fault segments ([Huang et al., 2017](#); [Cirella et al., 2018](#); [Scognamiglio et al., 2018](#)) and slip repetition on the same fault (in agreement with surface slip, [Civico et al., 2018](#); [Villani et al., 2018](#); [Brozzetti et al., 2019](#)). The fine-scale structure of the fault system with many intersecting and interacting faults has been outlined by the high-precision absolute and relative locations ([Michele et al., 2020](#); [Improta et al., 2019](#); [Tan et al., 2021](#); [Waldhauser et al., 2021](#)). We further investigate the role of fault rheology, by comparing the distribution of the coseismic slip and aftershocks to the Poisson ratio (ν) 3D pattern. The Poisson ratio, a proxy of rock rigidity, is directly derived from the newly computed velocity model applying the relationship: $\nu = [(V_p/V_s)^2/2 - 1]/[(V_p/V_s)^2 - 1]$ (i.e., [Stein and](#)

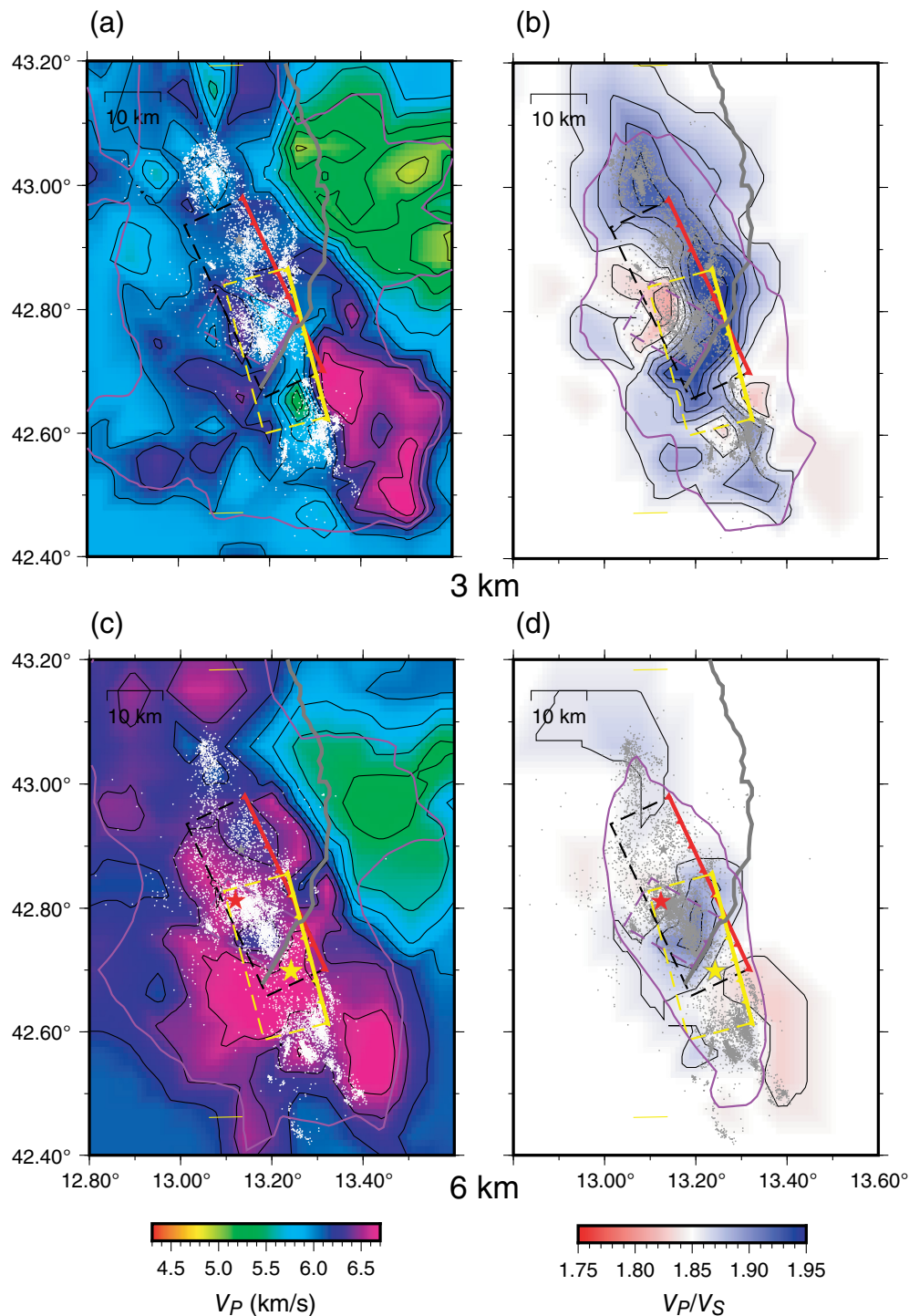
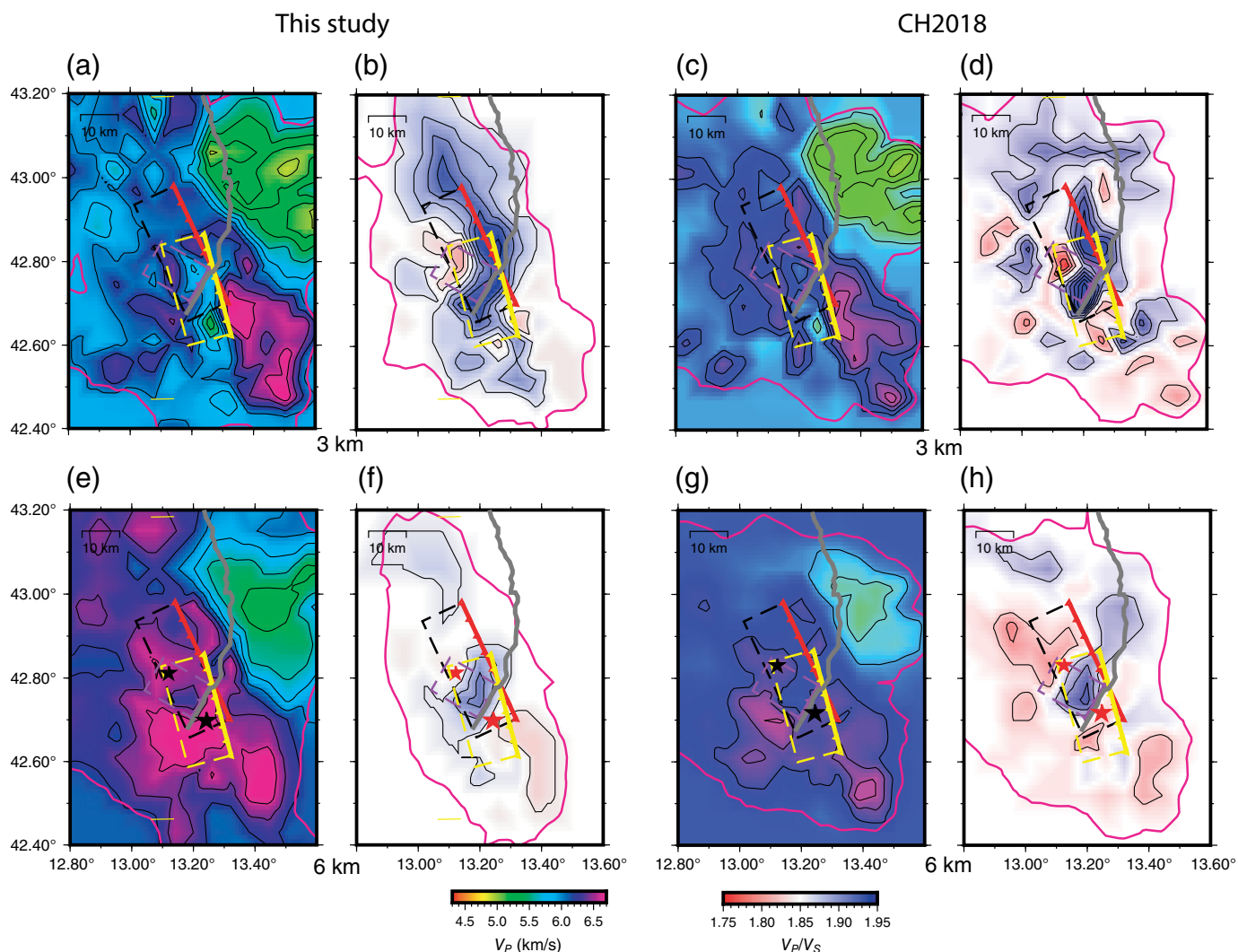


Figure 6. Layers of (a,c) V_p and (b,d) V_p/V_s at 3 and 6 km depth. Mainshocks hypocenters (red indicates M_w 6.5 and yellow indicates M_w 6.1 stars) and aftershocks (white or gray) are shown along with the box of the main faults modeled (red and purple for the M_w 6.5 mainshock from Scognamiglio *et al.*, 2018; and yellow indicates the M_w 6.1 mainshock from Cirella *et al.*, 2018). The gray line is the Sibillini thrust. Note the high- V_p/V_s body confined within the Sibillini thrust sheet. The purple lines indicate the well-resolved volume. Earthquakes occurring ± 1.5 km from the horizontal layers are shown. The color version of this figure is available only in the electronic edition.

Wyession, 2009). To this end, we draw down-dip sections of v along the fault segments and plot the coseismic slip and aftershocks occurring within ± 1 km from the fault (Fig. 10a).

Tomograms and aftershocks distribution help describe some main features consistently with those studies:

1. The M_w 6.1 bilateral rupture developed on two distinct slip patches of a N165°-trending fault (Cirella *et al.*, 2018), whereas the coseismic slip is small closer to the hypocenter. Few aftershocks occurred closer and up-dip to the hypocenter and in the southern patch (Fig. 10b), when they spread diffusely in the northern portion of the fault, aligned on a west-southwest-dipping plane. The northward extent of the aftershocks is sharply limited by a northwest-dipping plane that we associate to the second N210°-trending fault plane ruptured during the M_w 6.5 mainshock as proposed by Scognamiglio *et al.* (2018). Relatively high v is observed in the northern slip patch ($v = 0.3, 0.31$), when the nucleation occurs at a high or low v contrast, and the southern patch corresponds to a relatively low v (0.29–0.30).
2. The M_w 6.5 earthquake originated on a N155°-trending fault, the southern termination for which seems to coincide with the northern portion of the M_w 6.1 fault, although the two sources were modeled with a slightly different fault azimuth (about 10° of difference). The main plane is well defined by aftershocks, and the bending



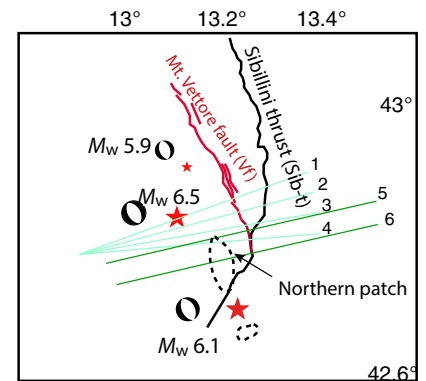
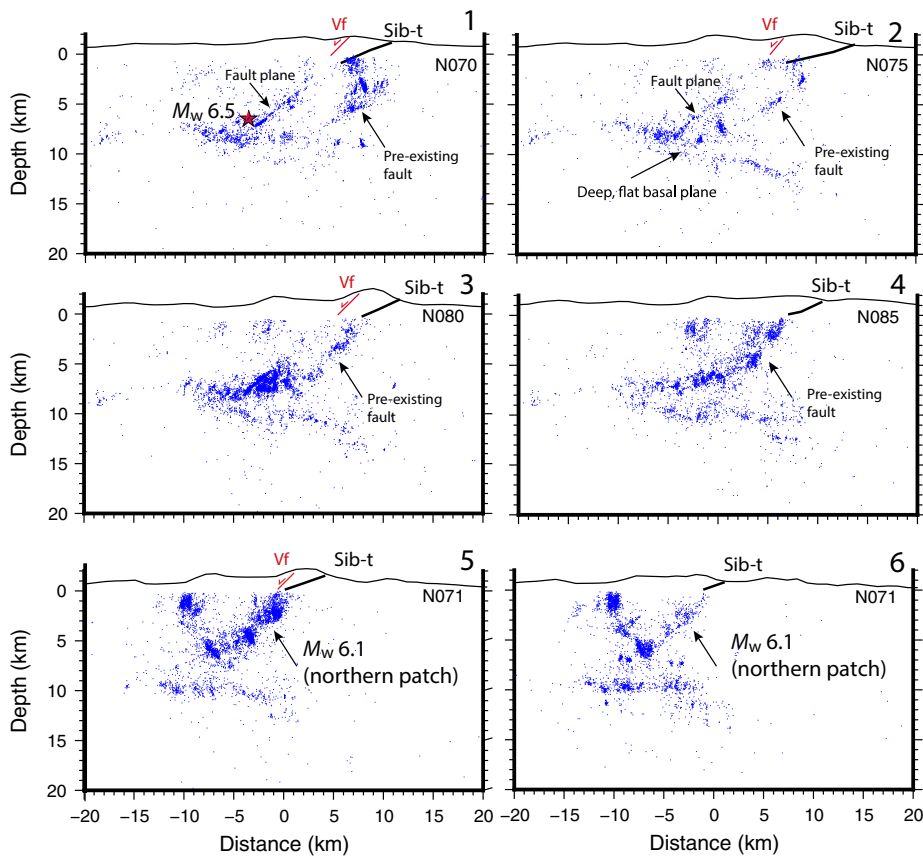
shown by aftershock distribution (Fig. 8) is consistent with the N210° secondary source proposed by Scognamiglio *et al.* (2018). The coseismic slip correlates with the relatively high ν patch on the fault ($\nu = 0.30, 0.31$, see Fig. 10c,d), in which the transient precursory velocity changes before the rupture were observed by Chiarabba *et al.* (2020). The hypocenter is located below than the main slip area in a low ν region, suggesting that enucleation took place within a rigid rock volume. The ground-motion time history has an initial emergent P -wave signal followed by an impulsive onset a few seconds later (Fig. 10e).

3. The hypocenters of the two mainshocks are located within a low ν volume, or at the high to low ν contrast, at a distance from the high coseismic slip that concentrates in the fault portions with $\nu > 0.3$.
4. The M_w 6.1 and 6.5 events ruptured a portion of the same fault, characterized by a relatively high ν (Fig. 10b,c). In this overlapping area, aftershocks of the first event are limited by the N210° transversal structure that acted as a barrier for the rupture evolution and aftershock migration (see also Waldhauser *et al.*, 2021). During the first two months,

Figure 7. Comparison between (a–d) our model and (e–h) the Chiarabba *et al.* (2018) model (CH2018) at 3 and 6 km depth. The Sibillini thrust (gray line), the mainshocks hypocenters, and the fault boxes are reported. The purple lines indicate the resolved volume as indicated by the spread function (SF) equal to 3, coherently to the threshold value used by Chiarabba *et al.* (2018). The color version of this figure is available only in the electronic edition.

- aftershocks were absent on the fault portion that experienced the higher coseismic slip during the second mainshock (i.e., the asperity, see Fig. 10b,c).
5. The M_w 5.9 Visso mainshock ruptured a shallow relatively high ν patch ($\nu = 0.3, 0.31$) to the northwest of the main asperity ruptured by the M_w 6.5 event.
6. Aftershocks surge off from the main faults, on inherited structures in the fault footwall and on a deep east-dipping plane (Fig. 8).

The heterogeneous distribution of aftershocks and coseismic slip of the two mainshocks correlates with a sharp variation of ν along the fault (Fig. 10), suggesting a strongly heterogeneous



behavior of the faults. The correlation between high coseismic slip and high ν suggests that the physical properties of the volume around the fault are important to constrain the slip behavior of faults. The high ν patches may correspond to portions of the fault in which the fluid pressure operates a dynamic drop of friction. This drop is high for the M_w 6.5 event and for the northern patch of the M_w 6.1 event, whereas it is lower for its southern patch, in agreement with the limited propagation of the rupture toward the south (Fig. 10).

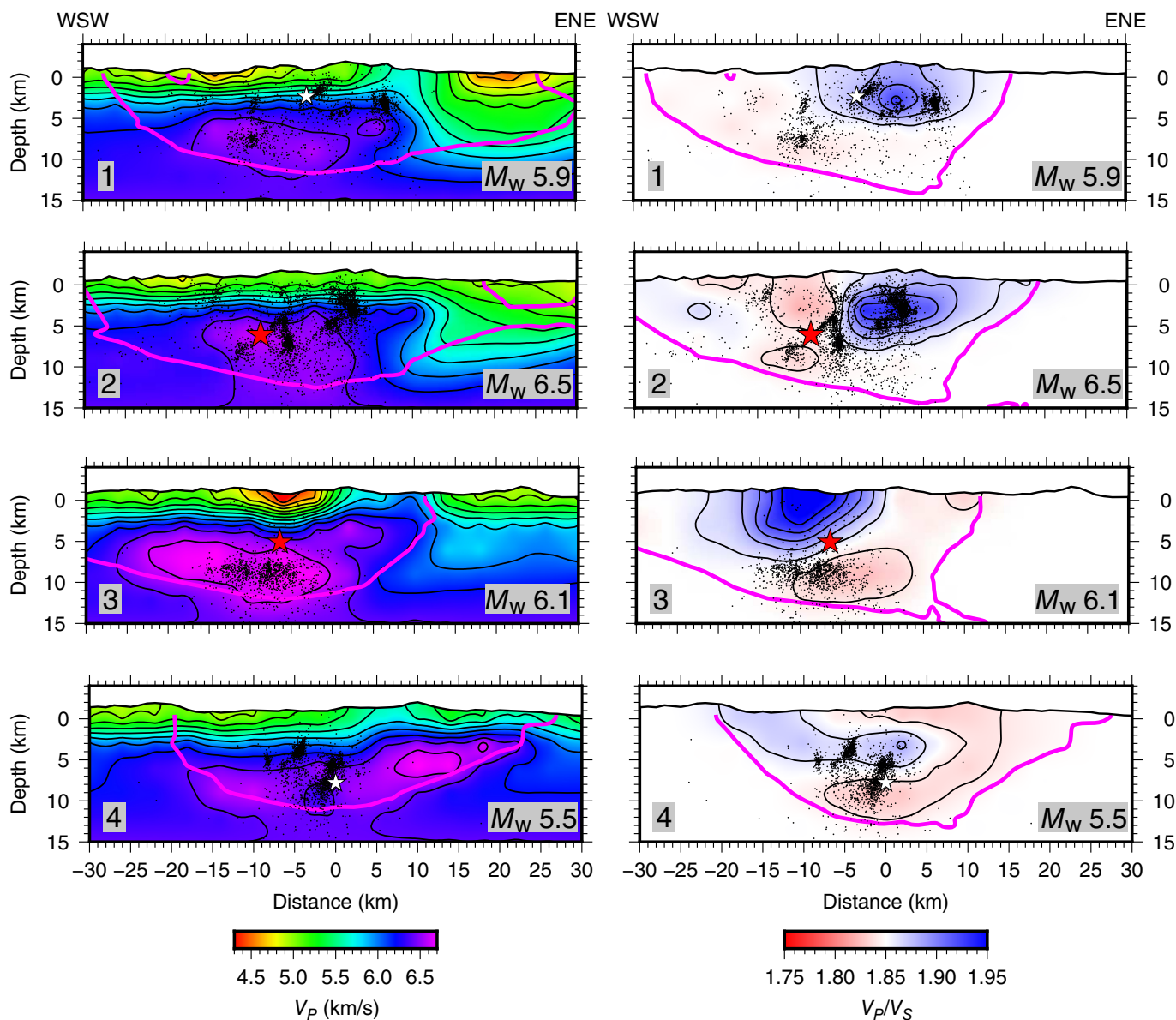
The M_w 6.1 event nucleated in a portion of low ν , with two patches of high slip having different ν values. To the south, the slip concentrated in a relatively low ν patch ($\nu = 0.29$ – 0.30), and aftershocks are poor; and to the north, the slip lies within a relatively high ν portion ($\nu = 0.30$ – 0.31) and vanishes at the limit of an exceptionally high ν patch ($\nu > 0.32$) in which the seismicity is abundant (Fig. 10b). We hypothesize that local conditions at the contrast between the lower and higher patches of Poisson ratio have conditioned the along-strike propagation of the rupture and the formation of the two main slip patches.

The M_w 6.5 rupture, the first phase of which was emergent (see the supplemental material and Fig. 10e), nucleated in a relatively low ν zone (0.28), whereas the large coseismic slip started when the propagation approached portions of the fault with higher ν values ($\nu = 0.30$ – 0.31 , Fig. 10c,d), with a similar process to the one observed for the 2009 L'Aquila mainshock. Significant slip (>0.5 m) extends to the south in the same area ruptured during the first mainshock. The slipped portion of the

Figure 8. Vertical sections of seismicity (DD locations from Waldhauser *et al.*, 2021 of the 3D catalog) that show the geometry and relative interaction between the two faults activated during the M_w 6.5 and 6.1 mainshocks (earthquakes occurring ± 0.3 km from the trace are shown). Note that sections 1–4, perpendicular to the M_w 6.5 fault, rotate southward, whereas sections 5 and 6 are perpendicular to the M_w 6.1 event. The red, bold, and light lines are the Sibillini thrust (Sib-t) and the Vettore-Bove normal fault (Vf) at the surface, respectively. The black arrows point to pre-existing faults of the compressive edifice present in the footwall of the Vettore fault. In the map, the traces of sections are shown. The dashed lines represent the 50 cm contouring of the surface projection of M_w 6.1 coseismic slip (Cirella *et al.*, 2018). Note that section 6 intersects the northern slip patch. The color version of this figure is available only in the electronic edition.

N210° fault has similar ν values, whereas the slip was absent close to the surface in the fault portion with very high values ($\nu > 0.32$). We hypothesize that the sharp change of ν along and down-dip the fault reflects rheological conditions of the material that influenced and interrupted the rupture propagation, delaying the onset of coseismic slip, and the failure of the main asperity.

Although part of the sharp change in V_p/V_s and ν can be attributed to a lithologic transition between the deep basement and the shallow limestone units, the sharp along-fault change (Fig. 10) is not attributable to a lateral change in lithology not



documented in the literature (Villani *et al.*, 2018 and references therein).

V_p/V_s anomalies are indicative of a different level of pore pressure (Wang and Nur, 1989; Dvorkin *et al.*, 1999) and/or pore types (Takei, 2002). We interpret the relatively high V_p/V_s and high ν patches as fluid-pressurized volumes of the fault in which stresses are accumulated and in which large coseismic slip occurred for the dynamic drop in effective friction, in agreement with laboratory studies (Di Toro *et al.*, 2011) and fault models (Noda and Lapusta, 2013).

On the contrary, mainshocks nucleation occurs within low ν rock volumes, in which the propagation of large amounts of slip is delayed and inhibited, consistent with the emergent onset on the first P -wave arrival. A similar pattern with an emergent, low-slip onset followed by large slip that correlate with changes in Poisson ratio (from low to high) was recognized for the M_w 6.1 L'Aquila event (Di Stefano *et al.*, 2011), suggesting this as one of

Figure 9. Cross sections of V_p and V_p/V_s tomography and relocated aftershocks close to the M_w 5.9 (white star), the M_w 6.5 (red star), the M_w 6.1 (red star), and the M_w 5.5 hypocenters (white star). Note the considerable amount of off-fault seismicity. Aftershock alignment for the M_w 5.9, the M_w 6.5, and the M_w 5.5 mainshocks define the fault plane on which the ruptures developed, whereas aftershocks are poor close to the hypocenter of the M_w 6.1 event. Seismicity on the basal plane occurs mostly within a high- V_p , low- V_p/V_s body. Earthquakes occurring within 1 km from the vertical planes are shown. The traces of sections numbered from 1 to 4 are drawn in Figure 1. The color version of this figure is available only in the electronic edition.

the possible nucleation mechanisms for moderate earthquakes hosted within carbonate rocks. The mapped changes of Poisson ratio seem to represent rheological discontinuities on the fault plane having a direct correlation and influence on the coseismic

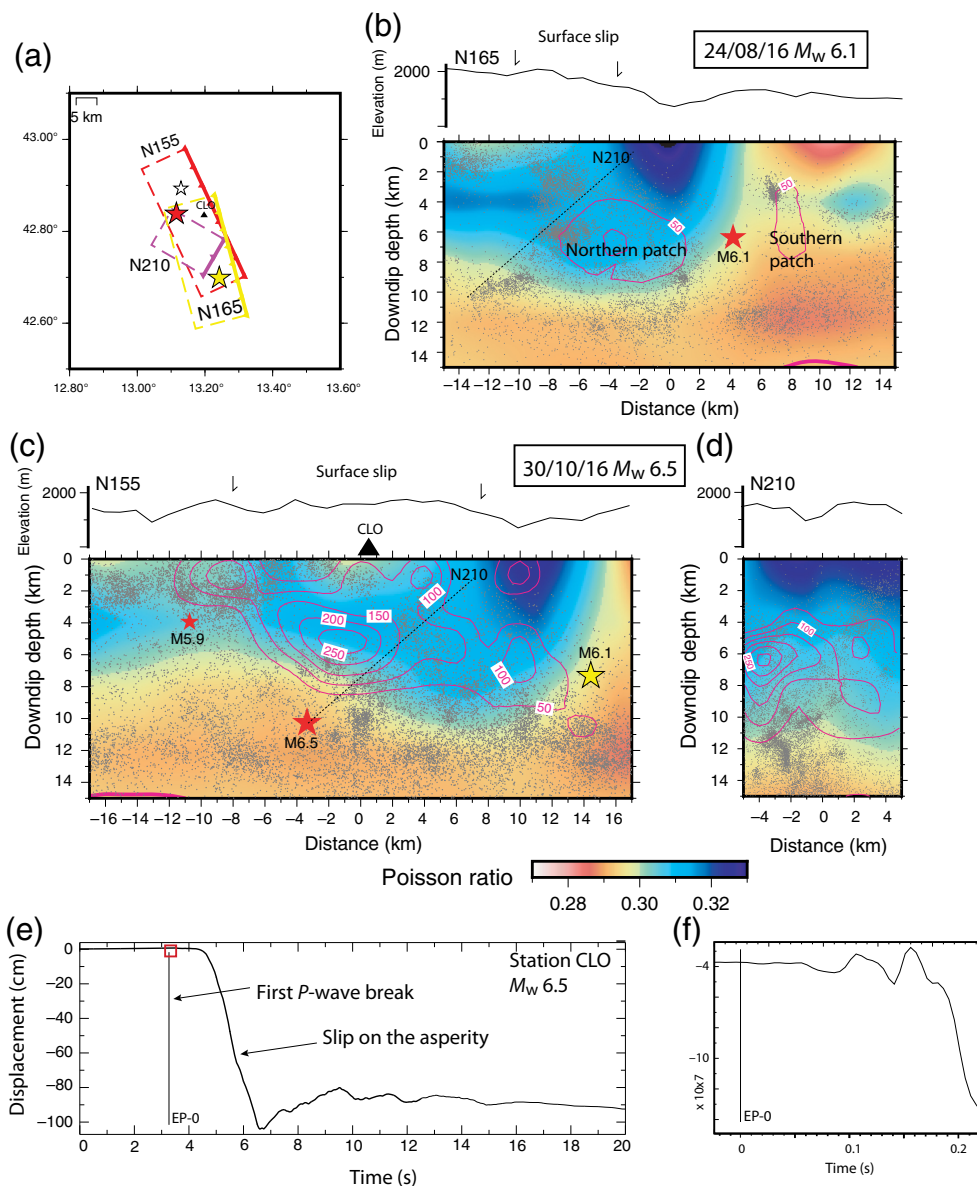


Figure 10. (a) Mainshocks locations (star) and surface projection of the main normal faults of the sequence: yellow indicates Amatrice M_w 6.1 fault, red indicates Norcia M_w 6.5 fault, and magenta indicates secondary fault of M_w 6.5 event. Fault geometry and coseismic slip are taken from [Cirella et al. \(2018\)](#) and [Scognamiglio et al. \(2018\)](#), for the two mainshocks, respectively. The triangle shows the CLO accelerometric station; (b) Poisson ratio distribution along the M_w 6.1 fault. Seismicity occurred before the 26 October M_w 5.9 event (3D-locations, gray dots), mainshock location (M_w 6.1, red star), and coseismic slip (cm, magenta lines) are shown. The thin black dotted line labeled $N210^\circ$ represents the trace of the secondary fault related to the M_w 6.5 mainshock ([Scognamiglio et al., 2018](#)); Note that early aftershocks stop within the high ν body at the location of the $N210^\circ$ segment. (c) Poisson ratio distribution along the M_w 6.5 fault. Aftershocks (3D locations, gray dots), mainshocks (M_w 6.5 and M_w 5.9, red stars, and M_w 6.1, yellow star) and M_w 6.5 coseismic slip (cm, magenta lines) are shown. The thin black

dotted line labeled $N210^\circ$ represents the trace of the secondary fault ([Scognamiglio et al., 2018](#)). The black triangle shows the position of the accelerometric station CLO. Large coseismic slip during the M_w 6.5 mainshock occurred within the high ν body (0.31), and part in the same portion slipped during the first M_w 6.1 event; (d) Poisson ratio distribution along the secondary fault of the M_w 6.5 mainshock ([Scognamiglio et al., 2018](#)). Aftershocks (3D locations, gray dots) and coseismic slip (cm, magenta lines) are shown. (e) Amplitude of coseismic displacement at station CLO (located 7.8 km away from the hypocenter) for the M_w 6.5 earthquake (further details in Figure SOM3). Note the delay of the large amplitude with respect to the starting of the rupture indicated by the bar of the P -wave first break; and (f) zoom on the P -wave first emergent break in the time window plotted with red box in panel (e). In panels (b), (c), and (d), only seismic events that occurred within ± 1 km from the fault plane are shown. The color version of this figure is available only in the electronic edition.

rupture history, as also hypothesized for the L'Aquila event (Di Stefano *et al.*, 2011; Cabrera and Poli, 2023).

The variable properties along the two mainshocks fault planes affected the coseismic rupture propagation and stop, acting respectively as fluid-based weakening mechanisms and barrier to aftershocks distribution. Contemporarily, overpressured fluids, compartmented within the older thrust system (Figs. 8 and 9), favor the dynamic weakening of the fault and the large coseismic slip.

A correlation of large across-fault V_p and V_p/V_s gradients with unstable slip behavior has been observed in the Parkfield segment of the San Andreas fault (Piana Agostinetti *et al.*, 2020) and interpreted as a different attitude to sustain elevated pore pressure in fault zones. We propose that the along-fault changes of material properties highlight a different attitude in sustaining the fluid pressure of different sectors of the fault.

We observe a spread of seismicity over a broad area after the first mainshock (Figs. 8 and 9), close and around the hypocenter of the second mainshock, that we are attracted to explain as due to the extreme fluid overpressure. The pervasive, shallow (depth <6 km), diffuse seismicity is probably promoted within the regions of sharp changes in material properties by the rough stress perturbation associated with complexity in rupture evolution. This observation agrees with the model of distributed seismicity controlled by shear-strain rate increase, and fluid overpressure that promoted widespread deformation within the Triassic evaporites, with ductile crustal deformation that caused distributed microseismicity (see Collettini *et al.*, 2022).

A striking feature evidenced by seismicity is the basal low-angle, east-dipping shear zone, in which the role in accommodating the extension and in the propagation of the major ruptures has been interpreted as active (Vuan *et al.*, 2017), passive (Tan *et al.*, 2021), and time-dependent (Sugan *et al.*, 2023). The shear-zone is located within a high- V_p , low- V_p/V_s (and hence high- V_s) volume that we speculate has a high strengthening behavior that impeded the development of large displacements during earthquakes.

Surface data and kinematic models suggest the repetition of coseismic slip during the two mainshocks on the same portion of the fault (see Villani *et al.*, 2018; Brozzetti *et al.*, 2019), although the relation between coseismic slip at depth and at the surface is never obvious. This could indicate an incomplete stress drop after the first event and/or dynamic effects on the rupture of the fault patch. Fast strength changes of faults have been proposed to explain the onset of small-magnitude seismicity, microearthquakes in laboratories (Passelègue *et al.*, 2016), and aftershocks during the passage of seismic waves (dynamic trigger, Gombert and Johnson, 2005), although still not documented for large ruptures. Because the ruptures of the two events are confined within high- V_p/V_s high- ν volumes, we hypothesize a dynamic drop of friction for high-fluid pressure. In this case, the impact on seismic hazard of repeated large ruptures on the same fault in short times is potentially strong.

Conclusions

The densely recorded 2016–2017 Amatrice-Norcia seismic sequence permits us to define how the rupture evolution is controlled by lateral changes of material properties on the same fault plane. Large coseismic slip occurs on fault patches with $\nu > 0.30$, possibly due to a drop of dynamic friction operated by fluid pressure. We observe an intense off-fault seismicity that we interpret as the activation of many small segments and pre-existing faults due to overpressurized fluid volumes. Finally, the repetition of slip on the same fault requires an incomplete stress release during M_w 6 events and/or a dynamic reloading of faults, for which impact in seismic hazard needs a deep evaluation.

Data and Resources

Seismograms analyzed in this study have been recorded during the 2016–2017 seismic sequence by permanent (Istituto Nazionale di Geofisica e Vulcanologia [INGV]) and temporary (INGV-British Geological Survey [BGS] survey) seismic stations. Earthquake data can be retrieved in the European Integrated Data Archive (EIDA) database (<http://eida.rm.ingv.it>, last accessed January 2023). Seismic tomography has been done with the Simulps14 code (Haslinger, 1998). Figures were made using Generic Mapping Tools (GMT) software (Wessel *et al.*, 2013). In the supplemental material, we show details of the resolution analysis and the pick of the emergent phase of the M_w 6.5 mainshock.

Declaration of Competing Interests

The authors acknowledge that there are no conflicts of interest recorded.

Acknowledgments

The research has been executed with internal Istituto Nazionale di Geofisica e Vulcanologia (INGV) funds. The authors thank the editors and two anonymous reviewers for their useful comments.

References

- Albertini, G., and D. S. Kammer (2017). Off-fault heterogeneities promote supershear transition of dynamic mode II cracks, *J. Geophys. Res.* **122**, 6625–6641, doi: [10.1002/2017JB014301](https://doi.org/10.1002/2017JB014301).
- Ben-Zion, Y., and C. G. Sammis (2003). Characterization of fault zones, *Pure Appl. Geophys.* **160**, 677–715.
- Beroza, G. C., and P. Spudich (1988). Linearized inversion for fault rupture behavior: Application to the 1984 Morgan Hill, California, earthquake, *J. Geophys. Res.* **93**, no. B6, 2156–2202, doi: [10.1029/JB093iB06p06275](https://doi.org/10.1029/JB093iB06p06275).
- Brozzetti, F., P. Boncio, D. Cirillo, F. Ferrarini, R. De Nardis, A. Testa, and G. Lavecchia (2019). High-resolution field mapping and analysis of the August–October 2016 coseismic surface faulting (central Italy earthquakes): Slip distribution, parameterization, and comparison with global earthquakes, *Tectonics* **38**, no. 2, 417–439, doi: [10.1029/2018TC005305](https://doi.org/10.1029/2018TC005305).
- Bruhat, L., Z. Fang, and E. M. Dunham (2016). Rupture complexity and the supershear transition on rough faults, *J. Geophys. Res.* **121**, doi: [10.1002/2015JB012512](https://doi.org/10.1002/2015JB012512).
- Cabrera, L., and P. Poli (2023). A struggled rupture initiation of the M_w 6.1 2009 L'Aquila earthquake, *Geophys. Res. Lett.* **50**, e2022GL102337, doi: [10.1029/2022GL102337](https://doi.org/10.1029/2022GL102337).

- Cheloni, D., V. De Novellis, M. Albano, A. Antonioli, M. Anzidei, S. Atzori, and R. Castaldo (2017). Geodetic model of the 2016 Central Italy earthquake sequence inferred from InSAR and GPS data, *Geophys. Res. Lett.* **44**, no. 13, 6778–6787.
- Chiarabba, C., P. De Gori, M. Cattaneo, D. Spallarossa, and M. Segou (2018). Faults geometry and the role of fluids in the 2016–2017 Central Italy seismic sequence, *Geophys. Res. Lett.* **45**, doi: [10.1029/2018GL077485](https://doi.org/10.1029/2018GL077485).
- Chiarabba, C., P. De Gori, M. Segou, and M. Cattaneo (2020). Seismic velocity precursors to the 2016 Mw 6.5 Norcia (Italy) earthquake, *Geology* **48**, doi: [10.1130/G47048.1](https://doi.org/10.1130/G47048.1).
- Chiaraluca, L., R. Di Stefano, E. Tinti, L. Scognamiglio, M. Michele, E. Casarotti, M. Cattaneo, P. De Gori, C. Chiarabba, G. Monachesi, et al. (2017). The 2016 central Italy seismic sequence: A first look at the mainshocks, aftershocks, and source models, *Seismol. Res. Lett.* **88**, no. 3, 757–771, doi: [10.1785/0220160221](https://doi.org/10.1785/0220160221).
- Chiaraluca, L., M. Michele, F. Waldhauser, Y. J. Tan, M. Herrmann, D. Spallarossa, G. C. Beroza, M. Cattaneo, C. Chiarabba, P. De Gori, et al. (2022). A comprehensive suite of earthquake catalogues for the 2016–2017 Central Italy seismic sequence, *Sci. Data* doi: [10.1038/s41597-022-01827-z](https://doi.org/10.1038/s41597-022-01827-z).
- Cirella, A., G. Pezzo, and A. Piatanesi (2018). Rupture kinematics and structural-rheological control of the 2016 Mw 6.1 Amatrice (central Italy) earthquake from joint inversion of seismic and geodetic data, *Geophys. Res. Lett.* **45**, 12,302–12,311.
- Civico, R., S. Pucci, F. Villani, L. Pizzimenti, P. M. De Martini, R. Nappi, and Open EMERGEO Working Group (2018). Surface ruptures following the 30 October 2016 M_w 6.5 Norcia earthquake, central Italy, *J. Maps* **14**, 151–160, doi: [10.1080/17445647.2018.1441756](https://doi.org/10.1080/17445647.2018.1441756).
- Collettini, C., M. R. Barchi, N. De Paola, F. Trippetta, and E. Tinti (2022). Rock and fault rheology explain differences between on fault and distributed seismicity, *Nat. Commun.* **13**, 5627, doi: [10.1038/s41467-022-33373-y](https://doi.org/10.1038/s41467-022-33373-y).
- Dieterich, J. H., and D. E. Smith (2009). Nonplanar faults: Mechanics of slip and off-fault damage, *Pure Appl. Geophys.* **166**, no. 10, 1799–1815, doi: [10.1007/s00024-009-0517-y](https://doi.org/10.1007/s00024-009-0517-y).
- Di Stefano, R., C. Chiarabba, L. Chiaraluca, M. Cocco, P. De Gori, D. Piccinini, and L. Valoroso (2011). Fault zone properties affecting the rupture evolution of the 2009 (Mw 6.1) L'Aquila earthquake (central Italy): Insights from seismic tomography, *Geophys. Res. Lett.* **38**, doi: [10.1029/2011gl047365](https://doi.org/10.1029/2011gl047365).
- Di Toro, G., R. Han, T. Hirose, N. De Paola, S. Nielsen, K. Mizoguchi, F. Ferri, M. Cocco, and T. Shimamoto (2011). Fault lubrication during earthquakes, *Nature* **471**, 494–498, doi: [10.1038/nature09838](https://doi.org/10.1038/nature09838).
- Dvorkin, J., G. Mavko, and A. Nur (1999). Overpressure detection from compressional- and shear wave data, *Geophys. Res. Lett.* **26**, 3417–3420, doi: [10.1029/1999GL008382](https://doi.org/10.1029/1999GL008382).
- Eberhart-Phillips, D. (1990). Three-dimensional P and S velocity structure in the Coalinga region, California, *J. Geophys. Res.* **95**, 15,342–15,363.
- Eberhart-Phillips, D., and M. Reyners (1997). Continental subduction and three-dimensional crustal structure: The northern South Island, New Zealand, *J. Geophys. Res.* **102**, 11,843–11,861.
- Fang, Z., and E. M. Dunham (2013). Additional shear resistance from fault roughness and stress levels on geometrically complex faults, *J. Geophys. Res.* **118**, 3642–3654, doi: [10.1002/jgrb.50262](https://doi.org/10.1002/jgrb.50262).
- Gomberg, J., and P. A. Johnson (2005). Dynamic triggering of earthquakes, *Nature* **437**, no. 4060, 830, doi: [10.1038/437830a](https://doi.org/10.1038/437830a).
- Haslinger, F. (1998). Velocity structure, seismicity and seismotectonics of northwestern Greece between the Gulf of Arta and Zakynthos, *Ph.D. Thesis*, Department of Geophysics, ETH, Zurich, Switzerland.
- Heaton, T. H. (1982). The 1971 San Fernando earthquake: a double event? *Bull. Seismol. Soc. Am.* **72**, 2037–2062.
- Huang, M. H., E. J. Fielding, C. Liang, P. Milillo, D. Bekaert, D. Dreger, and J. Salzer (2017). Coseismic deformation and triggered landslides of the 2016 Mw 6.2 Amatrice earthquake in Italy, *Geophys. Res. Lett.* **44**, no. 3, 1266–1274, doi: [10.1002/2016GL071687](https://doi.org/10.1002/2016GL071687).
- Improta, L., P. De Gori, and C. Chiarabba (2014). New insights into crustal structure, Cenozoic magmatism, CO₂ degassing, and seismogenesis in the southern Apennines and Irpinia region from local earthquake tomography, *J. Geophys. Res.* **119**, 8283–8311, doi: [10.1002/2013JB010890](https://doi.org/10.1002/2013JB010890).
- Improta, L., D. Latorre, L. Margheriti, A. Nardi, A. Marchetti, A. M. Lombardi, B. Castello, F. Villani, M. G. Ciaccio, F. M. Mele, et al. (2019). Multi-segment rupture of the 2016 Amatrice–Visso–Norcia seismic sequence (central Italy) constrained by the first high-quality catalog of early aftershocks, *Sci. Rep.* **9**, no. 1, 1–13, doi: [10.1038/s41598-019-43393-2](https://doi.org/10.1038/s41598-019-43393-2).
- Liu, X., and D. Zhao (2018). Upper and lower plate controls on the great 2011 Tohoku-Oki earthquake, *Sci. Adv.* **4**, eaat4396, doi: [10.1126/sciadv.aat4396](https://doi.org/10.1126/sciadv.aat4396).
- Mai, P. M., and G. C. Beroza (2002). A spatial random field model to characterize complexity in earthquake slip, *J. Geophys. Res.* **107**, no. B11, 2308, doi: [10.1029/2001JB000588](https://doi.org/10.1029/2001JB000588).
- Mendoza, C., and S. Hartzell (1988). Aftershock patterns and main shock faulting, *Bull. Seismol. Soc. Am.* **78**, 1438–1449.
- Michael, A. J., and D. Eberhart-Phillips (1991). Relations among fault behavior, subsurface geology, and three-dimensional velocity models, *Science* **253**, 651–654, doi: [10.1126/science.253.5020.651](https://doi.org/10.1126/science.253.5020.651).
- Michele, M., L. Chiaraluca, R. Di Stefano, and F. Waldhauser (2020). Fine-scale structure of the 2016–2017 Central Italy seismic sequence from data recorded at the Italian National network, *J. Geophys. Res.* **125**, no. 4, e2019JB018440, doi: [10.1029/2019JB018440](https://doi.org/10.1029/2019JB018440).
- Michelini, A., and T. V. McEvilly (1991). Seismological studies at Parkfield, part I: Simultaneous inversion for velocity structure and hypocenters using cubic B-splines parameterization, *Bull. Seismol. Soc. Am.* **81**, 524–552.
- Noda, H., and N. Lapusta (2013). Stable creeping fault segments can become destructive as a result of dynamic weakening, *Nature* **493**, 518–521, doi: [10.1038/nature11703](https://doi.org/10.1038/nature11703).
- Passelègue, F. X., A. Schubnel, S. Nielsen, H. S. Bhat, D. Deldicque, and R. Madariaga (2016). Dynamic rupture processes inferred from laboratory microearthquakes, *J. Geophys. Res.* **121**, 4343–4365, doi: [10.1002/2015JB012694](https://doi.org/10.1002/2015JB012694).
- Piana Agostinetti, N., G. Giacomuzzi, and C. Chiarabba (2020). Across-fault velocity gradients and slip behavior of the San Andreas Fault near Parkfield, *Geophys. Res. Lett.* **47**, doi: [10.1029/2019GL084480](https://doi.org/10.1029/2019GL084480).
- Reasenber, P., and W. Ellsworth (1982). Aftershocks of the Coyote Lake, California, earthquake of August 6, 1979 a detailed study, *J. Geophys. Res.* **87**, 10,637–10,655. doi: [10.1029/JB087iB13p10637](https://doi.org/10.1029/JB087iB13p10637).
- Scognamiglio, L., E. Tinti, E. Casarotti, S. Pucci, F. Villani, M. Cocco, F. Magnoni, A. Michelini, and D. Dreger (2018). Complex fault

- geometry and rupture dynamics of the MW 6.5, 30 October 2016, Central Italy earthquake, *J. Geophys. Res.* **123**, no. 4, 2943–2964.
- Shi, Z., and S. M. Day (2013). Rupture dynamics and ground motion from 3-D rough-fault simulations, *J. Geophys. Res.* **118**, 1122–1141, doi: [10.1002/jgrb.50094](https://doi.org/10.1002/jgrb.50094).
- Spallarossa, D., M. Cattaneo, D. Scafidi, M. Michele, L. Chiaraluca, M. Segou, and I. G. Maini, (2021). An automatically generated high resolution earthquake catalogue for the 2016–2017 central Italy seismic sequence, including P and S phase arrival times, *Geophys. J. Int.* **225**, 555–571.
- Sugan, M., S. Campanella, L. Chiaraluca, M. Michele, and A. Vuan (2023). The unlocking process leading to the 2016 Central Italy seismic sequence, *Geophys. Res. Lett.* **50**, e2022GL101838, doi: [10.1029/2022GL101838](https://doi.org/10.1029/2022GL101838).
- Stein, S., and M. Wysession (2009). *An Introduction to Seismology, Earthquakes, and Earth Structure*, John Wiley & Sons, Hoboken, New Jersey.
- Takei, Y. (2002). Effect of pore geometry on Vp/Vs: From equilibrium geometry to crack, *J. Geophys. Res.* **107**, doi: [10.1029/2001JB000522](https://doi.org/10.1029/2001JB000522).
- Tan, Y. J., F. Waldhauser, W. L. Ellsworth, M. Zhang, W. Zhu, M. Michele, L. Chiaraluca, G. C. Beroza, and M. Segou (2021). Machine-learning-based high-resolution earthquake catalog reveals how complex fault structures were activated during the 2016–2017 central Italy sequence, *Seismic Rec.* **1**, no. 1, 11–19, doi: [10.1785/0320210001](https://doi.org/10.1785/0320210001).
- Thurber, C. H. (1983). Earthquake locations and three-dimensional crustal structure in the Coyote Lake area, central California, *J. Geophys. Res.* **88**, 8226–8236.
- Tinti, E., L. Scognamiglio, A. Michelini, and M. Cocco (2016). Slip heterogeneity and directivity of the ML 6.0, 2016, Amatrice earthquake estimated with rapid finite-fault inversion, *Geophys. Res. Lett.* **43**, 10,745–10,752, doi: [10.1002/2016GL071263](https://doi.org/10.1002/2016GL071263).
- Toomey, D. R., and G. R. Foulger (1989). Tomographic inversion of local earthquake data from the Hengill-Grensdalur central volcano complex, Iceland, *J. Geophys. Res.* **94**, 17,497–17,510.
- Villani, F., R. Civico, S. Pucci, L. Pizzimenti, R. Nappi, P. M. De Martini, and the Open EMERGEIO Working Group (2018). A database of the coseismic effects following the 30 October 2016 Norcia earthquake in Central Italy, *Sci. Data* **5**, 180,049, doi: [10.1038/sdata.2018.49](https://doi.org/10.1038/sdata.2018.49).
- Vuan, A., M. Sugan, L. Chiaraluca, and R. Di Stefano (2017). Loading rate variations along a midcrustal shear zone preceding the M_w 6.0 earthquake of 24 August 2016 in Central Italy, *Geophys. Res. Lett.* **44**, 12–70.
- Waldhauser, F., M. Michele, L. Chiaraluca, R. Di Stefano, and D. P. Schaff (2021). Fault planes, fault zone structure and detachment fragmentation resolved with high-precision aftershock locations of the 2016–2017 central Italy sequence, *Geophys. Res. Lett.* **48**, e2021GL092918, doi: [10.1029/2021GL092918](https://doi.org/10.1029/2021GL092918).
- Wang, Z., and A. M. Nur (1989). Seismic and acoustic velocities in reservoir rocks: Volume 2. Theoretical and model studies, *Soc. Expl. Geophys.*, Tulsa, Okla, Geophysics Reprint Series, no. 10, 457 pp.
- Wessel, P., W. H. Smith, R. Scharroo, J. Luis, and F. Wobbe (2013). Generic mapping tools: Improved version released, *Eos Trans. AGU* **94**, no. 45, 409–410.
- Zhao, D., and H. Negishi (1998). The 1995 Kobe earthquake: seismic image of the source zone and its implications for the rupture nucleation, *J. Geophys. Res.* **103**, 9967–9986, doi: [10.1029/97JB03670](https://doi.org/10.1029/97JB03670).

Manuscript received 6 September 2022
Published online 9 August 2023